International Journal of Optomechatronics

ISSN: (Print) (Online) Journal homepage: www.tandfonline.com/journals/uopt20

Control of a quasi-static MEMS Mirror for raster scanning projection applications

Riccardo Antonello, Roberto Oboe, Daniele D'Elia & Luca Molinari

To cite this article: Riccardo Antonello, Roberto Oboe, Daniele D'Elia & Luca Molinari (2024) Control of a quasi-static MEMS Mirror for raster scanning projection applications, International Journal of Optomechatronics, 18:1, 2386991, DOI: 10.1080/15599612.2024.2386991

To link to this article: https://doi.org/10.1080/15599612.2024.2386991

© 2024 The Author(s). Published with license by Taylor & Francis Group, LLC

Published online: 16 Aug 2024.

Submit your article to this journal

Article views: 617

View related articles

View Crossmark data

Full Terms & Conditions of access and use can be found at
https://www.tandfonline.com/action/journalInformation?journalCode=uopt20

INTERNATIONAL JOURNAL OF OPTOMECHATRONICS
2024, VOL. 18, NO. 1, 2386991
https://doi.org/10.1080/15599612.2024.2386991

Control of a quasi-static MEMS Mirror for raster scanning projection applications

Riccardo Antonello[a], Roberto Oboe[a], Daniele D'Elia[b], and Luca Molinari[b]

[a]Department of Management and Engineering, University of Padova, Vicenza, Italy; [b]MEMS and Sensor Group, STMicroelectronics, Italy

ABSTRACT
The angular motion of quasi-static micromirrors used for raster scanning projection applications is typically affected by undesired oscillations related to high-frequency resonant modes triggered by the sawtooth-like driving signal. This paper proposes a novel closed-loop tracking controller for improving the linearity of the trace motion, and hence the image brightness. It includes a feedforward action to achieve the required tracking performance under nominal conditions, and a feedback control for robustness against disturbances and other nonidealities. Notch filtering prevents resonance-induced ringing. The simplicity of the architecture enables an easy implementation on FPGA or ASIC. Experimental tests carried out on two different micromirrors with Lead-Zirconate-Titanate (PZT) piezoelectric actuation and piezoresistive sensing demonstrate an average linearity of 0.12% and reproducibility of 15 mdeg for sawtooth reference trajectories with up to 8 deg amplitude and 120 Hz frequency, thus meeting the performance requirements mandated by the standards for high-resolutions projection applications.

KEYWORDS
MEMS micromirrors; laser beam raster scanning systems; tracking control loops; piezoelectric actuation; piezoresistive sensing

1. Introduction

MEMS (short for microelectromechanical systems) micromirrors are miniaturized devices produced with microfabrication techniques, such as silicon micromachining, thin-film deposition, and lithography, incorporating all the mechanical, electrical and optical components required for the precise control over the direction of the reflected light.[1]

Because of their compact size, low power consumption, high precision, fast response times and low cost, they are becoming an enabling technology for a variety of applications that require a precise control of light. For example, in optical communication systems, they are used for efficient wavelength switching and optical signal routing in fiber–optic networks.[2,3] In display technologies, they serve as the core component of many portable screen projectors (pico-projectors) and digital light processors (DLP), where the reflected light is used to create high-resolution images on screens.[4–6] In biomedical imaging systems such as confocal microscopes and endoscopes, they are used to precisely steer and focus the light beam, enabling high-resolution imaging of biological samples and improved visualization during minimally invasive procedures.[7–9] In Light Detection and Ranging (LiDAR) systems they are used to precisely steer the laser beam in

CONTACT Riccardo Antonello riccardo.antonello@unipd.it Department of Management and Engineering, University of Padova, Vicenza, Italy.

© 2024 The Author(s). Published with license by Taylor & Francis Group, LLC
This is an Open Access article distributed under the terms of the Creative Commons Attribution License (http://creativecommons.org/licenses/by/4.0/), which permits unrestricted use, distribution, and reproduction in any medium, provided the original work is properly cited. The terms on which this article has been published allow the posting of the Accepted Manuscript in a repository by the author(s) or with their consent.

Nomenclature

MEMS	Microelectromechanical Systems	AFE	Analog Front-End
LiDAR	Light Detection and Ranging	ADC	Analog-to-Digital Converter
AR	Augmented Reality	DAC	Digital-to-Analog Converter
MR	Mixed Reality	ETFE	Empirical Transfer Function Estimate
VR	Virtual Reality	DTFT	Discrete-Time Fourier Transform
HMD	Head-Mounted Display	PID	Proportional-Integral-Derivative
HUD	Head-Up Display	FIR	Finite Impulse Response
VRD	Virtual Retinal Display	IIR	Infinite Impulse Response
RP	Retinal Projector	DOF	Degrees of Freedom
LBS	Laser Beam Scanner	FPGA	Field-Programmable Gate Array
AFM	Atomic Force Microscopy	ASIC	Application-Specific Integrated Circuit
PZT	Lead Zirconium Titanate	RMS	Root Mean Square
PZR	Piezoresistor	ILC	Iterative Learning Control
PCB	Printed Circuit Board		

order to acquire an accurate real-time 3D scan of the surrounding environment, as required for applications of environment monitoring and mapping, obstacle detection, autonomous navigation.[10–13]

More recently, MEMS mirrors are finding new interesting applications in the growing fields of Augmented, Mixed and Virtual Reality (AR/MR/VR).[14] Thanks to their compact size and low power consumption, they are well-suited for integration into devices such as head-mounted displays (HMDs) and smart glasses.[15,16] They are typically integrated in optical engines that project an informative image on top of a transparent display placed in the user's field of view, as in conventional head-up displays (HUDs), or directly into the user's retina, as in virtual retinal displays (VRDs) – also known as retinal scan displays (RSDs) or retinal projectors (RPs).[17] Other applications include laser beam scanners (LBS) for depth-sensing imaging systems installed onboard of AR/MR headsets.

The structure of a (tunable) MEMS micromirror consists of several key components that work together to ensure an accurate reorientation of the incident light beam.[1] The core element is the mirror plate, which serves to reflect the incoming light. It is typically a thin, flat surface made of a reflective material such as aluminum or gold. It can be designed in several shapes and sizes depending on the specific application. The mirror plate is connected to the surrounding structure by means of elastic suspensions such as hinges, flexural beams or torsional springs that enable the rotation around a single or a pair of orthogonal axes.

The actuation can be provided with several methods. Electrostatic actuation is the most common.[18] It consists to apply a voltage difference between two electrodes, in order to create an electrostatic force that causes the plate to tilt. Electrostatic actuators are relatively easy to fabricate, thanks to their simple structure – in their most simple configuration, they consist on a pair of movable conducting plates. However, to generate a reasonable attracting or repelling force, they typically require a high actuation voltage (up to 200 V) which affects the overall power consumption of the device. Moreover, even in preence of a high actuation voltage, they are unable to generate either large or fast motions – an electrostatically actuated MEMS LBS hardly exceeds a frame rate of 60 Hz and an opening angle of few degrees. Magnetic actuation has been proposed as an alternative solution to achieve larger opening angles with lower actuation voltages. It exploits the magnetic force arising from the interaction of magnetic elements integrated into the device, typically a movable coil placed within a static magnetic field.[19] Magnetic actuators pose several challenges in their fabrication, because of their complex structures, and the difficulties of integrating some of the magnetic materials into the standard microfabrication processes employed by the semiconductor industry. For this reason and other reliability concerns, they are rarely adopted for commercial products. Piezoelectric actuators represent a viable alternative, owing to

their large actuation force and efficiency.[20] Creep and hysteresis may affect the performance, but their effect can be partially mitigated by appropriate compensation strategies.[21,22]

A MEMS micromirror usually integrates all the control electronics needed for its correct operation. The mirror position can be controlled either in open or closed–loop: in the latter case, a position sensor is required to provide the feedback signal. Capacitive,[23] piezoelectric[24] and piezoresistive sensors[25] are the most common; in most rare cases optical[26] or acoustic sensors[27] can also be exploited. The micromirror structure is completed by an optical interface, consisting of optical fibers, lenses, collimators and other components required to orient and focus the incoming light onto the mirror plate, and to gather and bring all the reflected light into the optical output port.

The specific structure of a MEMS micromirror depends on its intended application. In raster scanning applications (e.g. micro projectors, LiDAR systems, barcode readers, Digital Light Processing 3D printers, etc.) a pair of single-axis micromirrors are more commonly used to create the raster pattern, even though a single biaxial mirror can sometimes be used for the purpose.[28] Their design is specialized according to the movement to be accomplished. The *resonant mirror* performs the horizontal scan by vibrating at its resonant frequency, typically in the order of tens of kHz. To improve the driving efficiency, it is designed to have a sharp resonance with a high Q–factor amplification (small damping factor). The driving signal can be as simple as a pulse or square wave matched with the resonance frequency. Because of the high Q–factor, the system behaves as a very selective bandpass filter, so that in practice the resulting motion will always be sinusoidal or almost sinusoidal.

The *linear* or *quasi-static mirror* performs instead the vertical scan. It is driven by a sawtooth waveform, whose linear ramp up and down portions are related to the trace and retrace phases of the projected frame. The period is defined by the image refresh rate, which usually ranges from 60 Hz to 120 Hz for display projector applications. At these very low operating frequencies the system amplification is modest, especially when compared to the high resonance gain exploited in resonant mirrors. This, combined with the need to have large reflecting surfaces, imposes to design mirrors with low torsional stiffness and bigger, less efficient actuators.

Linear mirrors are more difficult to control than resonant mirrors. While a resonant mirror can be operated even by a simple square-wave oscillator, a linear mirror requires a more complex driving circuit, that typically includes a digital–to–analog converter (DAC) and an analog driver. In order to impose a linear motion profile, the driving signal must be carefully generated to avoid the excitation of the lightly damped system resonances, and to possibly compensate for the nonlinear characteristics of the electromechanical dynamics.

Several open-loop or closed-loop solutions have been proposed in literature to serve for the purpose. The most common open-loop driving methods consist of designing an actuation signal that does not excite the main mechanical resonances. This typically requires to remove any sharp corner in the driving signal, in order to reduce the harmonic content in the high frequency range. For example, in[29–31] the peaks of a triangular wave driving signal are rounded with either a third or fifth-order polynomial interpolation, which corresponds to designing a trajectory with limited jerk.[32] More sophisticated techniques involve the design of frequency-shaped trajectories with minimized harmonic content in desired frequency bands, such as those around lightly damped resonances.[33] Other open-loop methods focus instead on reshaping a given driving signal with suitable command pre-filters. In[34] is proposed an adaptive pre-filter combined with a resistive current-limiting feedback to both suppress the oscillations induced by the mechanical resonances, and to compensate for the intrinsic actuation nonlinearity of a comb-driven electrostatic scanner. A different design is presented in[35] for suppression of the residual oscillations after point-to-point motions in a commercial gimbal-less two-axis MEMS mirror. It is based on the application of the well-known input shaping method,[36] which consists in the generation of a sequence of precisely timed pulses with destructively interfering responses, so that no residual oscillation remains after the application of the sequence. The same approach is adopted in[37] in the context of Atomic Force Microscopy

applications (AFM). Specifically, the triangular waveform with flattened peaks used for actuation can be obtained as the output of an input-shaping pre-filter driven by a signal with sharp corners.

The distinct advantage of open-loop designs lies in the absence of an embedded sensor, leading to implementations with reduced area occupation. However, this renders the solutions less robust against disturbances and parameter variations. In contrast, closed-loop solutions are less susceptible to such issues. Conventional closed-loop architectures with PID (proportional-integral-derivative) controllers are discussed in[38] for the case of a dual-axis gimbal-less MEMS mirror with electrostatic push-pull comb-drive actuation and optical sensing. A simple phase-lead compensator is instead proposed in[39] for the closed-loop control of the slow (linear) axis of a biaxial electromagentically-driven and piezoresistively-sensed MEMS scanning mirror. This simple yet effective approach is feasible because no relevant spurious resonances are present in the system frequency response. The main torsional mode is gain–stabilized by setting a control bandwidth larger than its resonance frequency. A cascaded closed-loop control structure is instead proposed in[40] for a linear MEMS mirror with piezoelectric actuation and piezoresistive sensing. The inner loop employs a derivative feedback to actively dampen the main torsional mode, eliminating the issue of position ringing. The outer controller consists of a double integrator for the ideal perfect tracking of a ramp-varying reference signal, along with a lead-compensator to stabilize the feedback loop with a sufficient phase margin. Additional notch filters are inserted in the feedback path to suppress possible oscillations induced by spurious resonances. This design is further elaborated in,[41] where the position feedback is obtained from a state observer modeled on the main torsional mode of the mirror. The aim is to eliminate from the feedback any artifact stemming from the spurious resonances, which is unrelated to the actual mirror tilt motion. Another observer–based design is proposed in[42] for a 2D micro-scanner with in-plane comb-drive actuation for the fast (resonant) axis, and out-of-plane staggered vertical comb-drive actuation for the slow (linear) axis. The controller uses an exact feedforward linearization to impose the desired motion under nominal conditions, and a PID–like stabilizing feedback plus an extended Luenberger observer to stabilize the system along the desired trajectory. This flatness-based control approach is reconsidered in,[29] where it is compared against a simpler feedforward with no stabilizing feedback, driven by a jerk–limited trajectory. The design is particularly effective for electrostatically driven mirrors, whose actuation nonlinearity can be linearized with a proper feedforward action. An interesting extension is presented in,[43] where a repetitive controller is incorporated into the flatness-based design. This add-on is particularly effective in improving the tracking accuracy of the periodic reference trajectories, by compensating for deviations due to model nonlinearities, such as stiffness variations of the elastic suspensions, or the nonlinear characteristic of the electrostatic actuation. Results show a remarkable error reduction of a factor 6.8 with a final linearity error of 0.37% for a 6 deg/10 Hz reference trajectory, and a reduction of a factor 13.3 with a final linearity error of 0.13% for a 6 deg/10 Hz sawtooth reference trajectory.

Many other advanced solutions are proposed in literature, but most of them are tailored to address a specific issue of the device to control, or are difficult to implement with limited hardware resources. The aim of this paper is to show that even with a more traditional control structure it is possible to achieve the performance requirements mandated by the high-resolutions HD720/HD1080 standards for raster projection applications.[28] The proposed solution consists of a two degrees–of–freedom (DOFs) architecture, with the feedback path designed to compensate for the mechanical resonances and the nonlinearity of the piezoelectric actuation, and the feedforward path exploited to attain the desired tracking performance. Both the feedback and feedforward compensators consist of standard bi-quadratic cells or FIR filters, facilitating their implementation on custom hardware such as FPGAs or ASICs. For their tuning, a simple, yet effective procedure for the fast identification of the system resonances is also proposed in the paper. Compared to similar works proposed in literature and related to same micromirror structure with piezoelectric actuation and piezoresitive sensing,[40,41,44,45] the approach presented in this paper demonstrates better overall performances on a wider range of operating conditions.

Specifically, it achieves an average linearity of 0.12% and reproducibility of 15 mdeg for sawtooth reference trajectories with up to 8 deg amplitude and 120 Hz frequency.

The rest of the paper is organized as follows. Section 2 describes the electromechanical structure of the MEMS micromirrors considered in this study, and provides all the relevant modeling aspects required for the subsequent control design. Section 3 covers all the design details related to the proposed control architecture. The procedure conceived for the fast identification of the mechanical resonances is also described here. The results of the experimental tests carried out with two different micromirrors structures on a wide range of operating conditions are presented in Section 4. Final remarks and conclusions are reported in Section 5.

2. Micromirror description and modeling

2.1. Micromirror under test

The structure of the MEMS micromirrors considered in this paper is schematically depicted in Figure 1. Each mirror consists of a reflective plate (silicon plate with Aluminum coating) anchored to the substrate by means of two torsional beam suspensions that enable the rotation around its minor symmetry axis. Two different form factors of 2.50 mm × 1.44 mm (Mirror 1) and 2 mm × 3 mm (Mirror 2) are considered for the tests. The die photos of the two mirrors are shown in Figure 2(a) (Mirror 1) and Figure 2(b) (Mirror 2), respectively.

The actuation is provided by a set of four piezoelectric actuators connected to the four corners of the plate via folded springs. Each actuator consists of a silicon cantilever covered with a thin film (2 μ m) of Lead Zirconium Titanate (PZT) oxide sandwiched between two electrodes. The cantilevers bends outward of the mirror plane when a bias voltage is applied to them, thus generating an out-of-plane displacement at the corresponding plate corner. The mirror is tilted by applying the same bias voltage to the actuators on the same side of the plate midline, and opposite voltages to those located on opposite sides. The two opposite–phase voltages V_1 and V_2 required to drive the two actuator pairs are generated with a high–voltage amplifier. Up to 40 V are required to generate a tilt angle of nearly 8 deg, corresponding to a field–of–view of 32 deg.

The tilting motion of the plate is sensed with a set of four n-type silicon piezoresistors (PZRs), arranged in a Wheastone bridge configuration, and diffused at the anchor point of

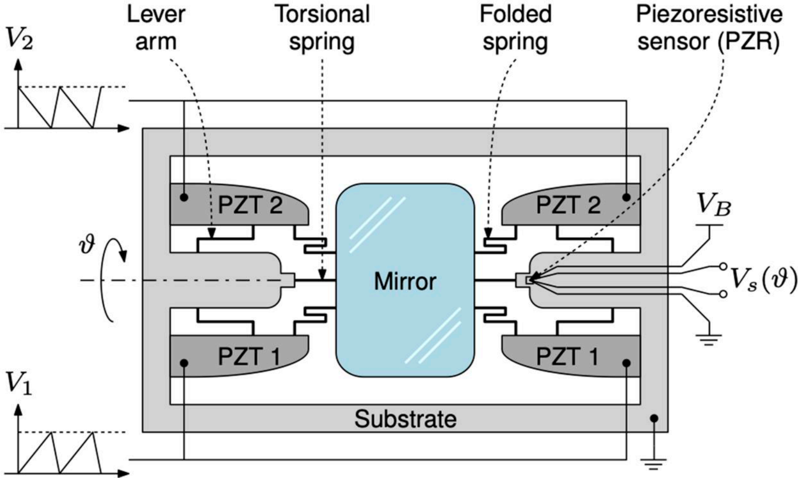

Figure 1. Schematic top-view of the quasi-static MEMS micromirror with PZT actuation and PZR sensing.

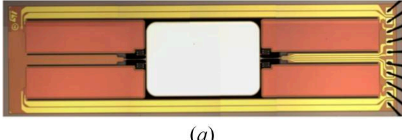

(*a*)

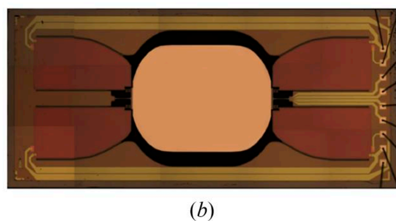

(*b*)

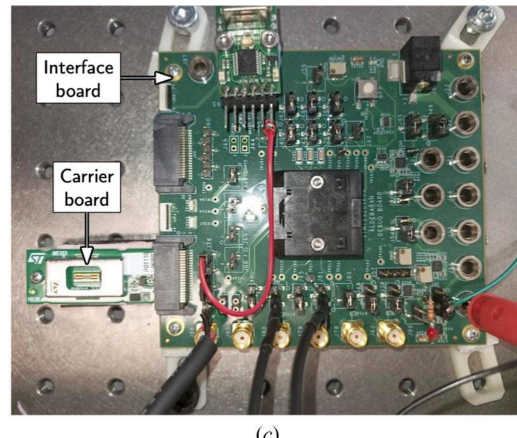

(*c*)

Figure 2. Hardware details: (a) Mirror 1 die photo; (b) Mirror 2 die photo; (c) interface board.

one of the torsional springs. The mechanical stress induced by the plate motion on the supporting spring causes an unbalancing of the values of the four PZRs, that can be detected as a voltage variation $V_s(\vartheta)$ at the bridge output, once this is biased with a proper voltage V_B (order of 3 V).

The micromirror is installed on a carrier printed circuit board (PCB) that simplifies the handling of the device during the experimental tests (see Figure 2(*c*)). It includes an Analog Front-End (AFE) to amplify the unbalanced voltage of the Wheastone bridge, and a card-edge connector for the installation on an FPGA–based interface and control board (see Figure 2(*c*)). The AFE consists of an instrumentation amplifier with programmable gain and an integrated compensation of both temperature and output bias (following an initial calibration). The interface board contains the high-voltage piezo-driver, consisting of a fully differential amplifier operating with a supply voltage of 40 V. The onboard FPGA can be used to control the micromirror. Alternatively, as done in this paper, the controller can be implemented on an external unit which directly interfaces with the piezo-driver and the AFE. A National Instruments PXI computer equipped with high resolution (16 bits) Analog-to-Digital (ADC) and Digital-to-Analog (DAC) converters has been used for the purpose, as shown in Figure 3.

2.2. System modeling

The typical frequency response from the sampled piezo driver input u to the sampled AFE output y is shown in Figure 4(*a*) (Mirror 1) and Figure 4(*b*) (Mirror 2). The Empirical Transfer Function Estimate (ETFE)[46] has been obtained first, as the ratio between the output and input Discrete Time Fourier Transforms (DTFTs). The input has been chosen as a normally distributed white noise excitation with standard deviation $\sigma = 0.1$ V, sampled at a rate of 50 kHz. Several mechanical modes couple at the PZR output. For Mirror 1, the first resonance at about 1 kHz corresponds to the main torsional mode. The remaining resonances are related to spurious modes, among which the most relevant are an in-plane mirror translation at about 6.1 kHz and the actuator vibration at nearly 9.3 kHz. Since the Mirror 2 has a bigger reflective plate, the main torsional mode has a lower resonant frequency, at about 565 Hz. Other relevant spurious modes are an out-of-plane mirror translation at approximately 5 kHz, and actuator vibrating modes at about 8 kHz and 14.2 kHz. Results have been confirmed by extensive finite element simulations and vibrometry inspections.[40]

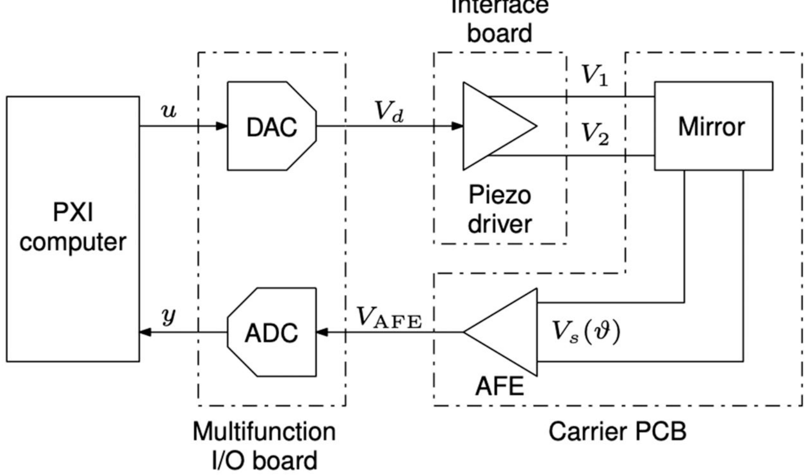

Figure 3. Testing system architecture.

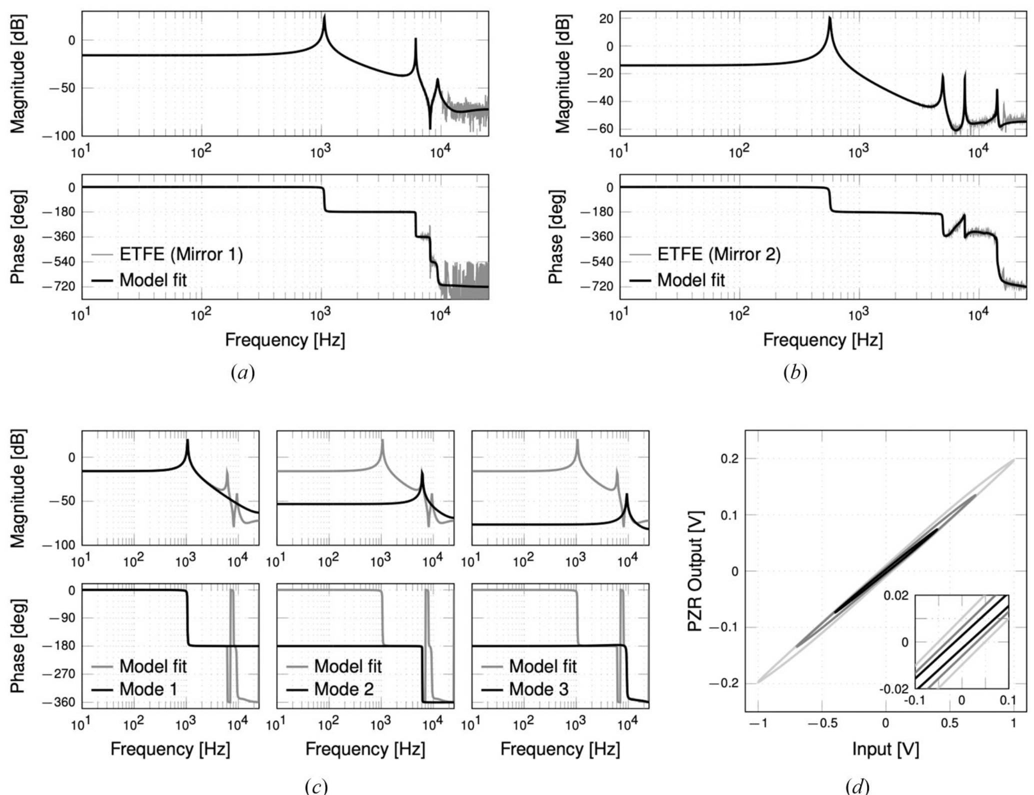

Figure 4. Identification of the quasi-static and dynamic responses: (a,b) least squares fitting of the parametric model to ETFE data; (c) Bode plots of the modal expansion terms (Mirror 1); (d) actuation hysteresis loop for three different levels of the driving voltage (Mirror 1). *Note*: Bode plots shown in figure do not account for the unit delay introduced by the D/A conversion.

A parametric model has then been fitted on the ETFE data using least-square methods. The model has been selected as a discrete-time transfer function $P(z)$ with enough poles and zeros to fit all the relevant resonances in the frequency response. An additional unit delay has been added to account for the time delay of the D/A conversion in the experimental system. In modal expansion form, the transfer function is:

$$P(z) = \sum_{i=1}^{N} P_{me_i}(z) = \sum_{i=1}^{N} \frac{r_{0_i}}{z^2 + c_{1_i} z + c_{0_i}} \tag{1}$$

As an example, the Bode plots of the three modal expansion terms related to the modeling of Mirror 1 are shown in Figure 4(c).

The linear time-invariant (LTI) model (1) does not account for nonidealities such as the hysteretic behaviour of the piezoelectric actuation, the second-order dependence of the modal stiffness on the mirror tilt angle, and the (linear) dependence of the PZR sensitivity on temperature. The latter twos are documented in.[40] The hysteresis in the quasi–static response is instead shown in Figure 4(d). It has been obtained by measuring the PZR output in response to slowly varying sinusoidal inputs with different amplitude.

Since the hysteresis curve is relatively narrow, and its midline is almost linear except for minor deviations at the extremal points, its impact on the behaviour predicted by (1) is limited. Nonetheless, as noticed in the experimental tests, it can lead to an underestimation of the static gain predicted by the ETFE method, negatively impacting on the the control design. The correct gain can be found with ad-hoc tests, e.g. by measuring the steady-state output amplification of a slowly-varying sinusoidal input signal. The responses in Figures 4(a) and 4(b) account for this correction.

3. Micromirror control

3.1. Control system design

In raster scanning applications such as display projectors, the tilt angle of the quasi-static micromirror of Sec. 2 is controlled to track a sawtooth reference waveform with specified amplitude and frequency, where the former depends on the desired maximum field–of–view (FOV), while the latter defines the image refresh rate. The ramp up and down portions of the sawtooth waveform are related to trace and retrace phases of the projected image. The retrace time is chosen as short as possible, in order to minimize the loss of image brightness.

During the trace phase, the main control goal is to track the linear motion profile without triggering spurious oscillations, as this reflects in an image brightness modulation, i.e., image bands

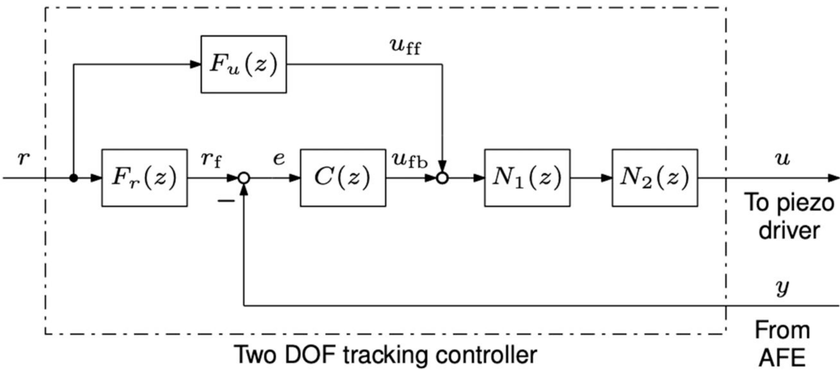

Figure 5. Control system architecture.

with different brightness. On the other hand, in the retrace phase the goal is to bring the mirror back to the original position without overshooting, as this causes a bright band at image top.

Figure 5 shows the block diagram of the control system designed to achieve such goals. It consists of a two degrees-of-freedom (DOF) tracking controller, where the feedforward compensators $F_r(z)$ and $F_u(z)$ are used to achieve the desired tracking performances under nominal conditions, while the feedback controller $C(z)$ adds robustness against disturbances and model uncertainties. Some notch filters are employed to perform a gain compensation of the spurious mechanical resonances, in order to prevent a possible mode spillover instability of the feedback loop.[47] For Mirror 1 two notch filters $N_1(z)$ and $N_2(z)$ are sufficient to target the 2nd and 3rd mechanical resonance; for Mirror 2 a third notch filter is required to compensate the extra spurious resonance at 14.2 kHz. The controller is designed to operate at a 50 kHz sampling rate. This value is selected to be sufficiently larger than the selected control bandwidth (order of kHz – see next), but not too large compared to the center frequency of the two notch filters, otherwise numerical issues could arise during their discretization and implementation.[48] In addition, the selected sampling frequency has to be compatible with the limitation imposed by the hardware, namely the computer running the controller in real time, and the data acquisition board (see Figure 3). The feasible range for the control command u is ± 1 V, as exceeding these values would saturate the piezo driver, causing distortions in the resulting motion profile. The details of the control design are reported next. For convenience, the design is illustrated for Mirror 1, but an identical procedure applies also to Mirror 2:

1. *Notch filters* $N_1(z)$ *and* $N_2(s)$: they are obtained by discretizing two continuous–time counterparts with transfer functions:

$$N_i(s) = \frac{s^2 + 2\delta_i \omega_i s + \omega_i^2}{s^2 + 2\delta_i' \omega_i s + \omega_i^2} \qquad (i = 1, 2) \tag{2}$$

The notch frequency ω_i and the damping factor δ_i of the complex zeros are selected to match the frequency and damping factor of the resonance to compensate for. These can be estimated with the methods of Sec. 2.2 or, alternatively, with the multi–tone identification method presented in Sec. 3.2. The damping factor δ_i' of the complex poles is instead selected to obtain a sufficiently wide stop-band, in order to accommodate for possible variations of the resonance frequency (order of $\pm 10\%$ of the nominal value, as observed in preliminary characterizations of a few samples[40]), but not too wide, especially for the first notch filter $N_1(s)$, otherwise the feedback controller would be unable to totally recover the phase lag introduced by the notch filter, and the resulting phase margin would be unsatisfactory. Trial and error is somehow necessary, as no systematic design procedures are available. However, for lightly damped resonances, damping factors one to two orders of magnitude larger than those of the targeted resonances typically yield satisfactory results. Another design criteria for the damping factors δ_i' would be to find the values that better equalize the phase response of the series of the two notch filters with that of a pure delay. This approach aims to facilitate the design of the feedforward compensation, as demonstrated next. The actual values of the parameters are reported in Table 1.

The discretization of (2) is performed with the *matched pole–zero* method,[48] in order to preserve the notch frequency in the discretization process. The discretized filters are:

$$N_1(z) = \frac{0.8932(z^2 - 1.431z + 0.9987)}{z^2 - 1.286z + 0.7931} \tag{3}$$

Table 1. Notch filter parameters.

i	$f_i = \frac{\omega_i}{2\pi}$ [kHz]	δ_i	δ_i'
1	6.149	0.9×10^{-3}	0.15
2	9.369	10.3×10^{-3}	0.20

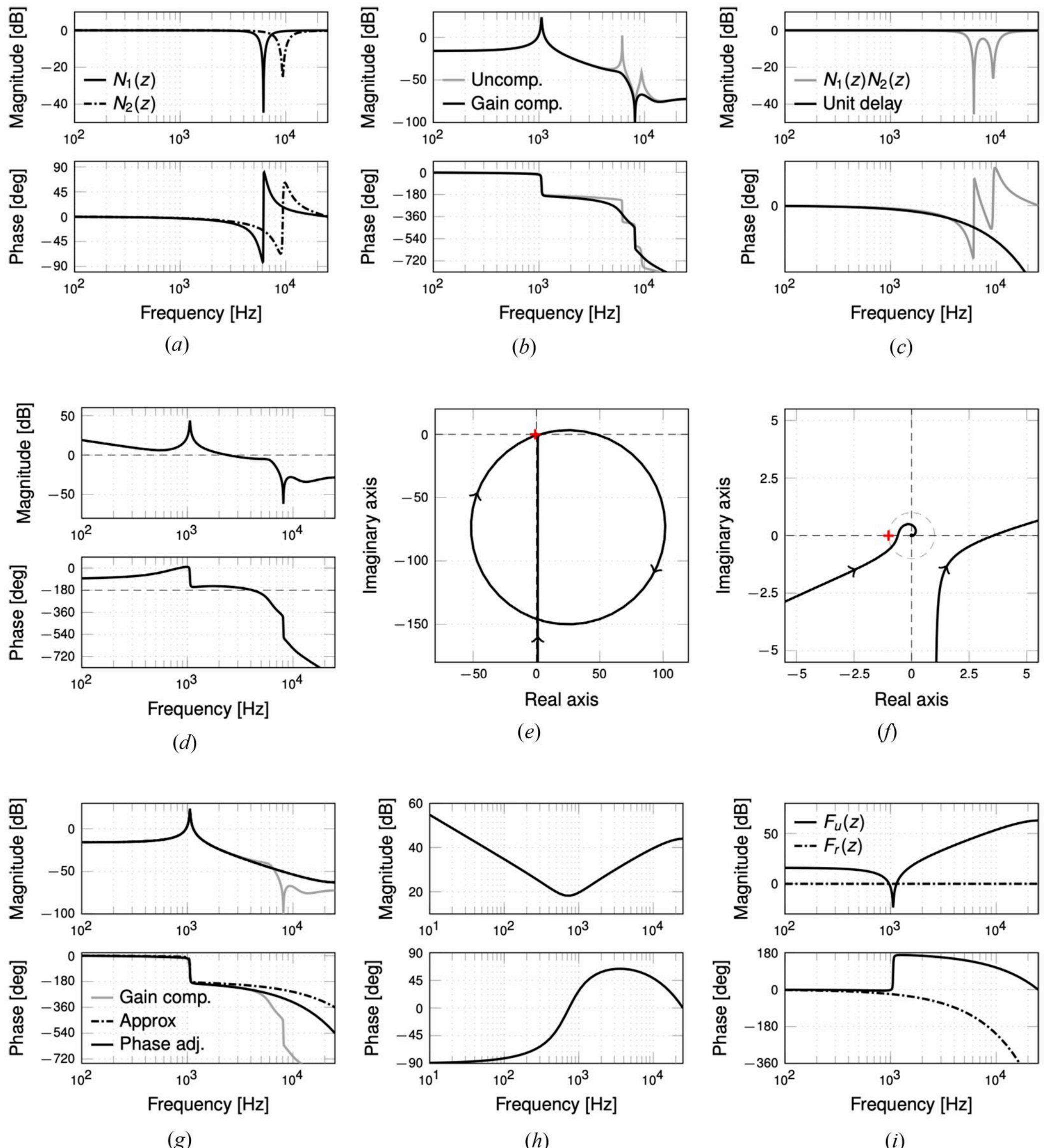

Figure 6. Control system design (Mirror 1): (a) notch filters; (b) uncompensated vs gain-compensated plant (micromirror); (c) notch filters series vs unit delay; (d–f) loop transfer function (Bode and Nyquist plots); (g) approximations of the gain-compensated plant (for feedforward compensation design); (h) feedback controller; (i) feedforward compensators.

$$N_2(z) \quad = \frac{0.8076(z^2 - 0.7575z + 0.9759)}{z^2 - 0.6404z + 0.6244}$$

The Bode plots are shown in Figure 6(*a*); the Bode plot of the gain–compensated plant, namely $P(z)N_2(z)N_1(z)$, is instead reported in Figure 6(*b*).

2) *Feedback controller* $C(z)$: it is designed with loopshaping techniques, to achieve a gain crossover frequency $f_{gc} = \omega_{gc}/2\pi \approx 2.3\,\text{kHz}$ and a phase margin $\varphi_m \approx 30^\circ$. The former is selected (mostly by trial and error) to obtain a good rejection of disturbances and other non idealities, without producing an excessive amplification of the measurement noise, or the saturation of the

control command. It is also chosen to prevent the instability caused by the spillover of high–frequency resonances not compensated by notch filtering. Note that the first resonance is within the control bandwidth, and has to be phase–stabilized by the feedback controller. The actual value of the phase margin is chosen as the maximum achievable with the selected controller structure, namely a proportional–integral–derivative (PID) controller. The design is performed by emulation, considering the following continuous-time implementation:

$$C(s) = K_P\left(1 + \frac{1}{sT_I} + \frac{sT_D}{T_L s + 1}\right) \tag{4}$$

The time constant T_L of the derivative action is selected to have a cut–off frequency of 15 kHz (i.e., $1/T_L = 2\pi \times 15\,\text{kHz}$). The ratio between the integral and derivative times is set as $\alpha = T_I/T_D = 1.0$ to have a pair of complex conjugate zeros, which yields a rapid phase recovery in the neighborhood of the imposed gain crossover frequency. The final discretized version of (4), obtained with the trapezoidal (Tustin) method to limit the phase distortion introduced by the discretization process, is equal to:

$$C(z) = \frac{70.657(z^2 - 1.9z + 0.9079)}{(z-1)(z-0.02961)} \tag{5}$$

The structure is rather simple, and can be implemented with a single bi–quadratic filter cell. The Bode plot is shown in Figure 6(*h*). The Bode and Nyquist plots of the resulting loop transfer function are instead reported in Figures 6(*d*)–6(*f*).

It is worth to point out that a PID controller with complex zeros has been preferred over an alternative solution based on an integrator plus some (i.e., 3) first–order phase lead compensators because of its simpler structure, and its better robustness in terms of gain margin. In fact, the former yields a –20 dB/dec slope at the 0 dB –crossing, since the gain crossover frequency ω_{gc} is located in a region where the plant has a –40 dB/dec roll–off, while the controller has a slope of +20 dB/dec (see also Figure 6(*h*)). On the other hand, an integrator plus 3 first–order phase–lead compensators would have in total a +40 dB/dec slope, that yields an almost flat 0 dB–crossing, and hence a modest or even negligible gain margin. It is also interesting to note that the tracking performance in the proposed solution is primarily achieved through feedforward compensation (under nominal conditions). As a result, the demands on the control bandwidth of the feedback controller are less stringent compared to a solution relying exclusively on feedback, as that presented in.[40,44,45]

3) *Feedforward compensators* $F_u(z)$ *and* $F_r(z)$: they are designed to closely match the response of a given reference model $M(z)$ from the position reference r to the measured output y (see Figure 5). The goal is achieved by setting:

$$F_u(z) = \frac{M(z)}{P_1(z)}, \qquad F_r(z) = M(z) \tag{6}$$

where $P_1(z)$ is an approximation of the gain–stabilized plant $P(z)N_1(z)N_2(z)$, obtained by considering the 1st term of the modal expansion (1), and then by:

- Adding an extra unit–delay z^{-1} to account for the phase distortion produced by the two notch filters. In fact, as also noticeable from Figure 6(*c*), the phase distortion produced by the series of the two notch filters is similar to that of a unit delay (at the selected sampling rate), at least in the frequency range relevant for the control design.
- Adjusting the DC gain to match that of the overall plant transfer function $P(z)$. The resulting transfer function is:

$$P_1(z) = \frac{0.003431}{z(z^2 - 1.981z + 0.9986)} \tag{7}$$

whose Bode plot is reported in Figure 6(g).

With a simple reference model consisting of only three unit–delays, i.e., $M(z) = z^{-3}$, the resulting feedforward compensators are:

$$\begin{aligned} F_u(z) &= \frac{353.79(z^2 - 1.981z + 0.9986)}{z^2} \\ F_r(z) &= z^{-3} \end{aligned} \tag{8}$$

The former consists of a FIR filter with two-taps, while the latter is a pure delay. The number of delays in the reference model is chosen to make the transfer function $F_u(z)$ of the command feedforward compensator at least proper, and hence physically implementable. The Bode plots of the two compensators are shown in Figure 6(i).

As the two feedforward compensators (8) do not introduce any attenuation at high frequency, the sawtooth reference waveform must be properly smoothed out to avoid the excitation of the uncompensated high frequency resonant modes. This is achieved by generating a reference signal with rounded corners, obtained by joining the trace and retrace linear profiles with a polynomial interpolant[29–31] (see Sec. 4). An alternative option would be to select the reference model as a low–pass filter with suitable roll–off and corner frequency, so that to introduce the required high–frequency attenuation in the feedforward compensators (6). For example, with the reference model:

$$M(z) = \frac{0.05654}{(z - 0.6162)^3} \tag{9}$$

the ideal response to a step speed reference (i.e., a linear position ramp) has a settling time at 1% of about 375 µs, which is the 5% of the trace time of a 120 Hz sawtooth reference with 90% – 10% trace-retrace ratio, and no overshoot. This agrees with the specification on the linearity error, as formalized in Sec. 4. Obviously, with (9) the complexity (order) of the feedforward compensators increases, and this could be a problem when the goal is to keep the design as simple as possible.

The overall complexity of the proposed design is very limited. Specifically, an implementation on FPGA or ASIC would require only three bi–quadratic IIR filter cells to implement the two notch filters $N_1(z)$ and $N_2(z)$ in (3) and the PID controller $C(z)$ in (5), along with a two–taps FIR filter and three unit delays for the feedforward compensators $F_u(z)$ and $F_r(z)$ in (8). On the contrary, the comparable implementation presented in[40,44,45] necessitates of at least two bi–quadratic IIR filter cells for mode shaping on the feedback path, as well as at least four single or bi-quadratic cells to implement the double integrator and the lead compensator in the feedback controller, and the derivative controller in the innner loop for the active damping of the main torsional resonant mode.

3.2. Control calibration

The best performances are attained when the design of Sec. 3.1 is tailored on the actual dynamic response of the device to be controlled. This implies that the identification of the parametric model (1) has to be repeated for every new device. The approach followed in Sec. 2.2 for the purpose is not very practical, as it requires the collection and processing of a large amount of data. Therefore, the alternative method described next has been developed to simplify and speed up the initial controller calibration procedure.

Given a multi-resonance system, the relevant parameters of each resonant mode of interest can be obtained by fitting the parametric model:

$$P_i(s) = \frac{K_i}{s^2 + 2\delta_i \omega_{n_i} s + \omega_{n_i}^2} \tag{10}$$

on some frequency response data points collected around the corresponding resonant peak. In detail:

1) Let $P(s)$ denote the transfer function of the multi–resonance system. For every resonance of interest, identify the frequency response magnitude $|P(j\omega)|$ on a set of N frequency points ω_k located around frequency of the resonance peak (see Figure 7(a)). Six points are usually sufficient to get reasonable results from the method.

Each magnitude point $|P(j\omega_k)|$ is identified by applying a sinusoidal excitation (*tone*) at the probing frequency ω_k, and then by evaluating the ratio:

$$|P(j\omega_k)| = Y_k / U_k \tag{11}$$

where U_k is the amplitude of the input tone, while Y_k is the amplitude of the output oscillation at steady–state (i.e., when the transient is over). The latter can be extracted from the system output measurement y with an envelope detector (see Figure 7(b)).

2) Around each resonance of interest, it is assumed that the frequency response $P(j\omega)$ can be approximated with that of the model (10), namely $P_i(j\omega)$. The unknown parameters of the latter are determined by fitting the magnitude response to the sample data (11) collected in the previous step. In order to use conventional linear least-squares methods, the inverse of the square magnitude is rewritten in the following regression form:

$$\frac{1}{|P_i(j\omega_k)|^2} = \boldsymbol{\varphi}_k^T \ \boldsymbol{\theta} \tag{12}$$

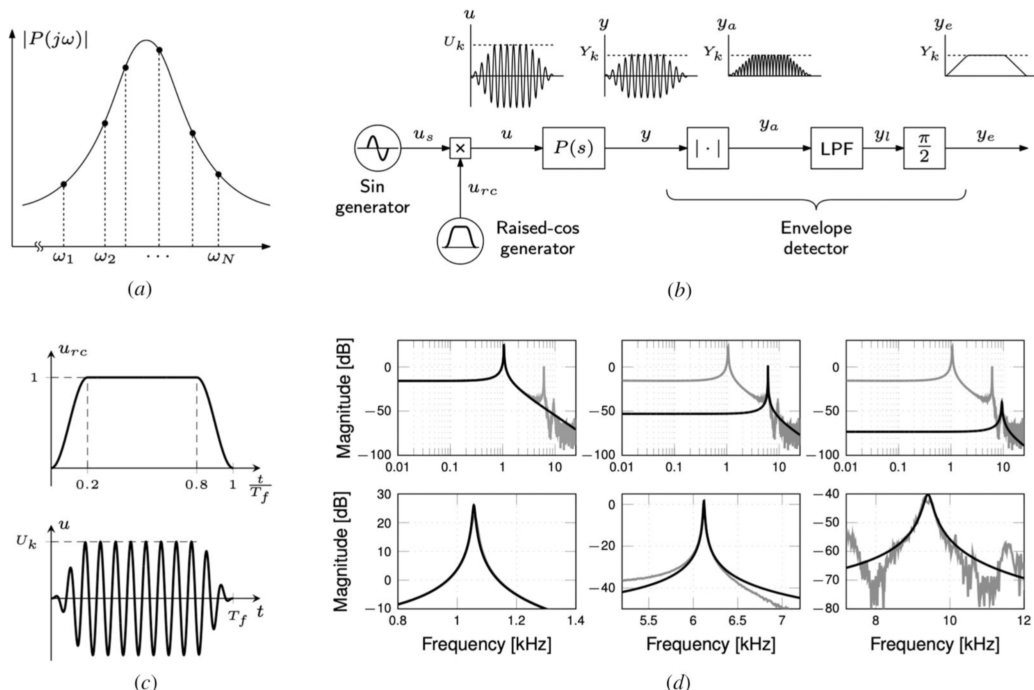

Figure 7. Multi–tone identification method: (a) sample points of the frequency response magnitude around a generic resonance peak; (b) frequency response probing circuit; (c) typical input tone (top: raised-cos weighting function; bottom: amplitude-modulated input tone); (d) multi–tone identification results (Mirror 1).

where $\boldsymbol{\varphi}_k = [\omega_k^4,\ \omega_k^2,\ 1]^T$ is the vector of regressors, and

$$\boldsymbol{\theta} = [\theta_1,\ \theta_2,\ \theta_3]^T = \left[\frac{1}{K_i^2},\ \frac{2(2\delta_i^2-1)\omega_{n_i}^2}{K_i^2},\ \frac{\omega_{n_i}^4}{K_i^2}\right]^T \tag{13}$$

is the vector of unknown parameters.

3) The least–squares estimate of the vector of unknown parameters is:

$$\hat{\boldsymbol{\theta}}_{LS} = \left[\hat{\theta}_1,\ \hat{\theta}_2,\ \hat{\theta}_3\right]^T = (\boldsymbol{\Phi}^T\boldsymbol{\Phi})^{-1}\boldsymbol{\Phi}^T\ \boldsymbol{Y} \tag{14}$$

where:

$$\boldsymbol{\Phi} = [\boldsymbol{\varphi}_1, \ldots, \boldsymbol{\varphi}_N]^T \ \in\ \mathbb{R}^{N\times 3} \tag{15}$$

$$\boldsymbol{Y} = \left[\frac{1}{|P(j\omega_1)|^2}, \ldots, \frac{1}{|P(j\omega_N)|^2}\right]^T \ \in\ \mathbb{R}^{N\times 1} \tag{16}$$

It is important to notice that the regressors matrix $\boldsymbol{\Phi}$ has a Vandermonde structure, which is notoriously ill conditioned. Better numerical conditioning can be obtained by resorting to a *weighted* formulation of the aforementioned least–squares problem, in which each column of $\boldsymbol{\Phi}$ is multiplied by the inverse of its last element.

4) The estimates of the parameters in (10) are obtained by inversion of the expressions in (13). It holds that:

$$\hat{K}_i = \frac{1}{\sqrt{\hat{\theta}_1}}, \quad \hat{\omega}_{n_i} = \sqrt[4]{\frac{\hat{\theta}_3}{\hat{\theta}_1}}, \quad \hat{\delta}_i = \sqrt{\frac{1}{2} + \frac{\hat{\theta}_2}{4\sqrt{\hat{\theta}_1\hat{\theta}_3}}} \tag{17}$$

For each mechanical resonance to identify, the probing frequencies are selected to cover a sufficiently wide range centered around the nominal value of the resonance frequency. The actual values used in the Mirror 1 case are reported in Table 2. They corresponds to $\pm 25\,$Hz, $\pm 75\,$Hz and $\pm 125\,$Hz deviations from the nominal value of each resonance frequency. In the test, each tone is applied for 1 s, but shorter time intervals can be considered, especially for high–frequency tones. The amplitudes are suitably selected for each resonance, with higher values for smaller resonant peaks. To ensure a seamless transition between two consecutive input tones and prevent the onset of undesired oscillations, the amplitude of each tone is modulated using a raised cosine window (see Figure 7(*c*)). The results of the identification are reported in Table 3. The estimated parameters are in good agreement with the corresponding nominal values, and the fitted models are well matched with the ETFE data of Sec. 2.2 (see Figure 7(*d*)). If necessary, especially in

Table 2. Multi–tone identification method (Mirror 1): input tones parameters (frequency f_k and amplitude U_k).

Resonance	$f_k = \frac{\omega_k}{2\pi}$ [Hz]						U_k [V]
1st	975	1025	1075	1125	1175	1225	0.01
2nd	5675	5725	5775	5825	5875	5925	0.15
3rd	9575	9625	9675	9725	9775	9825	1.50

Table 3. Estimated parameters (Mirror 1): ETFE + LS fitting / multi-tone.

Resonance	$f_{n_i} = \frac{\omega_{n_i}}{2\pi}$ [kHz]	$\delta_i = \frac{1}{2Q}$ [−] ($\times 10^{-3}$)	K_i [−] ($\times 10^{6}$)
1st	1.058/1.056	5.3/4.0	7.163/7.117
2nd	6.149/6.127	0.9/0.9	−3.282/ − 3.282
3rd	9.369/9.368	10.3/10.9	−0.523/ − 0.531

situations with noisy measurements, the estimates can be refined by re-applying the method on narrower probing frequency ranges.

4. Experimental results

The control design of Sec. 3.1 has been experimentally validated on the testing system shown in Figure 3 with rapid prototyping techniques. The controller of Figure 5 has been implemented in Simulink, and run in real-time on the PXI computer with the aid of the Simulink Desktop–Real Time toolbox. A smoothed sawtooth reference signal has been used for the tests, obtained by joining the linear ramps of the trace and retrace phases with a 7th–order polynomial interpolant. Two metrics have been used to assess the tracking performances:

a. *Linearity error* $L(t)$: it is determined by evaluating the deviation of the mirror position from a first-order polynomial fit during the constant speed portion of each trace (assumed as $[5\%, 95\%]$ portion of the total trace trace time), and then by averaging over multiple traces to remove the effect of noise. It quantifies how closely the mirror position follows a straight-line reference trajectory during the trace phase.
b. *Reproducibility error* $R(t)$: is defined as the standard deviation of the mirror position evaluated at the same fraction of the trace time (constant speed portion) over multiple periods of the reference signal. It quantifies how much the noise affects the intended straight-line motion during each trace phase.

To meet the standards of a high-resolution HD720/HD1080 projector,[28] the root mean square (RMS) of the linearity error, normalized to the full-scale motion range, must be below the 1% threshold. On the other hand, the reproducibility error must be below 25 mdeg.

Reference signals with different waveforms (sawtooth vs triangular), peak amplitude (up to 8 deg) and frequency (in the $[60 \ \text{deg}, 120 \ \text{deg}]$ range) have been considered for the tests. The typical response to a $6 \ \text{deg}/100\,\text{Hz}$ sawtooth/triangular reference signal is reported in Figure 8 (Mirror 1). The desired response y_d reported in the plots refers to the output of the reference model $M(z)$, and hence is a delayed version of the actual reference signal r provided to the control system. From Figures 8(b) and 8(e) it can be noticed how the constant speed portion of the trace time, delimited by the vertical dashed lines in figure, is approached with almost no overshoot. The linearity and reproducibility errors averaged over 100 periods are shown in Figures 8(c) and Figure 8(f). Both the performance metrics meet the design specifications. It is nevertheless important to remind that the two quantities are affected by the actual measurement noise on the testing system, which includes the quantization of the analog–to–digital conversion. Their values could be potentially lower for an implementation on dedicated hardware such as FPGA or ASIC. The results of the experimental tests for different reference waveforms, amplitudes and frequencies are summarized in Table 4 (Mirror 1) and Table 5 (Mirror 2). Better overall performances can be noticed for Mirror 1. The larger linearity errors observed for Mirror 2 are probably caused by the presence of less damped spurious modes, which makes the stabilization more problematic. Nevertheless, performances are well within the design specifications for all the tested operating conditions. For comparison purposes, in Table 6 are summarized the performances achieved by some recent works presented in literature. Unfortunately, they are obtained with different devices or testing conditions, so that establishing a fair comparison among them is challenging. Only the works presented in[40] and[41] refer to the same micromirrors consider in this paper, and can therefore be considered as a reference. Overall, the solution presented in this paper demonstrates superior performance across a broader spectrum of operating conditions.

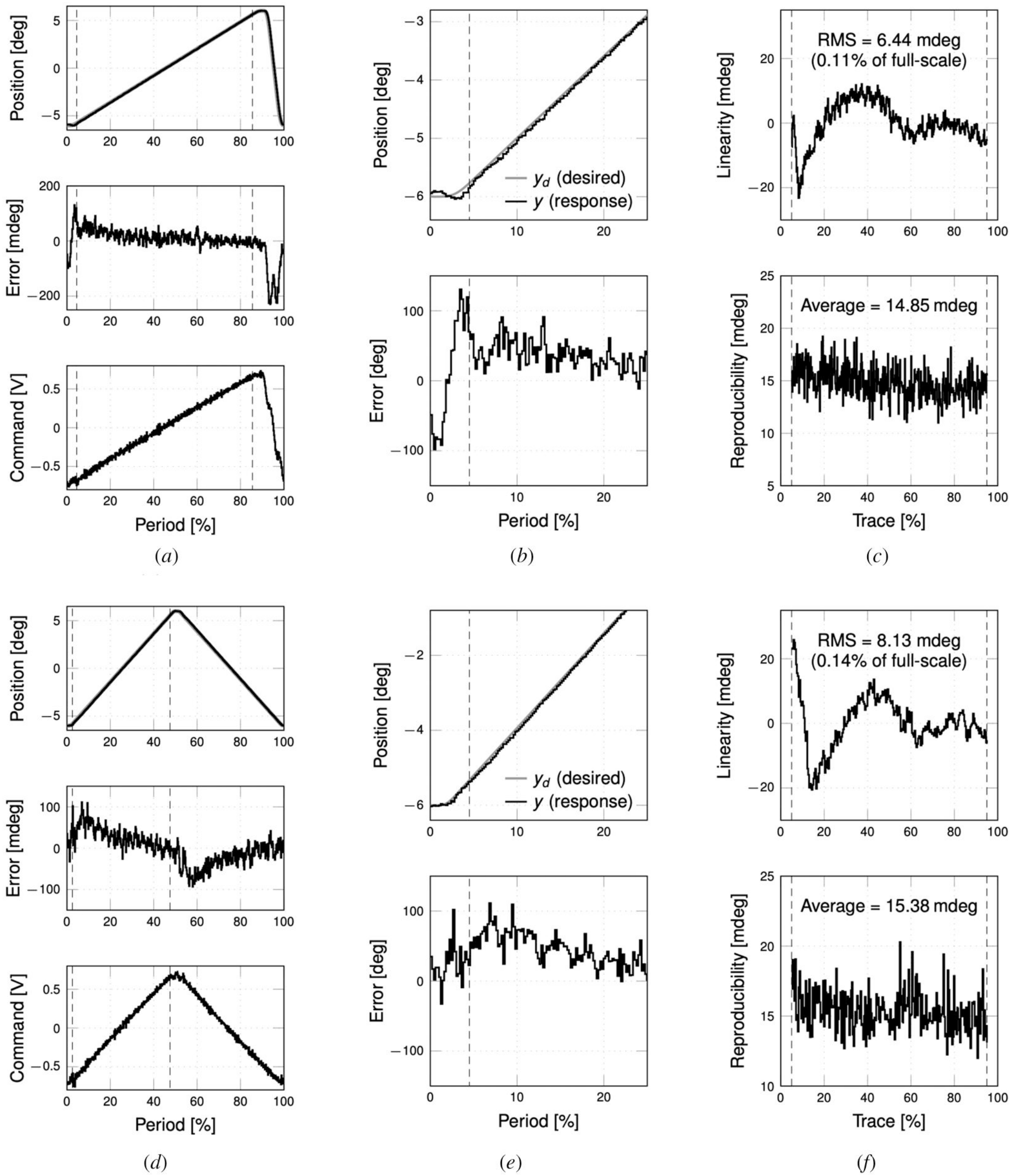

Figure 8. Experimental results (Mirror 1): (a,d) typical control response with a 6 deg/100 Hz sawtooth and triangular reference waveforms; (b, e) control response detail; (c, f) performance metrics (linearity and reproducibility errors). The portion of the trace considered for the evaluation of the performance metrics is delimited by vertical dashed lines.

Additional tests have been conducted to assess the robustness of the proposed design against variations of the most critical parameters of the mirror frequency response, specifically the resonance frequencies and the static (DC) gain. Tests have been performed in simulation with a numerical model of Mirror 1. Performance degradation was evaluated by applying a $\pm 10\%$ variation to the selected parameter. The results are collectively summarized in Table 7, for the case of a 6 deg/100 Hz sawtooth reference signal. For what concerns the stability of the feedback loop, the most critical variation is that related to the frequency of the second mechanical resonance, because it induces a mode spillover in the loop transfer function, as evident from the Bode plots

Table 4. Control performance (Mirror 1): Linearity [%] / Reproducibility [mdeg].

Sawtooth reference waveform

Reference frequency [Hz]	Reference amplitude [deg]			
	2	4	6	8
60	0.09/14.52	0.06/14.52	0.07/15.08	0.10/15.41
80	0.10/14.77	0.07/14.99	0.10/15.22	0.14/15.70
100	0.15/14.48	0.07/14.47	0.11/14.85	0.17/15.51
120	0.23/14.48	0.11/14.86	0.14/15.16	0.24/16.23

Triangular reference waveform

Reference frequency [Hz]	Reference amplitude [deg]			
	2	4	6	8
60	0.12/14.73	0.07/15.05	0.09/15.03	0.14/15.35
80	0.14/14.86	0.09/14.70	0.10/15.18	0.17/15.38
100	0.20/14.48	0.14/14.73	0.14/15.38	0.19/15.78
120	0.30/14.51	0.22/14.93	0.18/15.72	0.23/16.30

Table 5. Control performance (Mirror 2): Linearity [%] / Reproducibility [mdeg].

Sawtooth reference waveform

Reference frequency [Hz]	Reference amplitude [deg]			
	2	4	6	8
60	0.15/16.37	0.09/16.75	0.16/17.61	0.18/17.15
80	0.34/16.48	0.11/16.94	0.17/17.59	0.32/18.81
100	0.55/16.18	0.21/16.51	0.14/17.56	0.33/18.98
120	0.77/16.60	0.33/16.93	0.15/17.83	0.37/18.83

Triangular reference waveform

Reference frequency [Hz]	Reference amplitude [deg]			
	2	4	6	8
60	0.18/16.51	0.11/16.90	0.13/17.19	0.23/18.55
80	0.26/15.95	0.16/16.54	0.15/17.52	0.25/18.42
100	0.32/14.48	0.21/16.55	0.18/17.59	0.27/18.41
120	0.39/16.29	0.26/16.49	0.22/17.36	0.30/18.63

Table 6. Performance comparison with existing literature.

Reference	Linearity [%]	Linearity [mdeg]	Reproducibility [mdeg]	Notes
This work	0.12	6.3	15.02	Average of all the data reported Table 4.
[40]	0.18	14	25.5	with 60 Hz – 0.6 deg sawtooth reference.
[41]	–	0.03	15	sawtooth reference parameters not specified.
[30]	3.3	200	7	with 10 Hz – 7 deg triangular reference.
[29]	0.32	16	2	with 50 Hz – 5 deg triangular reference.
[49]	1.25	–	–	with 50 Hz – 8 deg sawtooth reference.
[39]	7	–	200	with 60 Hz – 0.4 deg sawtooth reference.
[43]	0.13	–	–	with 10 Hz – 6 deg sawtooth reference.

Table 7. Control performance in presence of parameter variations (Mirror 1 – simulations): Linearity [%]/ Reproducibility [mdeg].

Parameter variation	Parameter			
	ω_{n_1}	ω_{n_2}	ω_{n_3}	DC gain
−10%	0.08/18.05	0.06/21.69	0.05/19.63	0.19/18.54
+10%	0.06/21.71	unstable	0.04/18.97	0.10/19.91

Note: results are obtained with a 6 deg/100 Hz sawtooth reference signal.

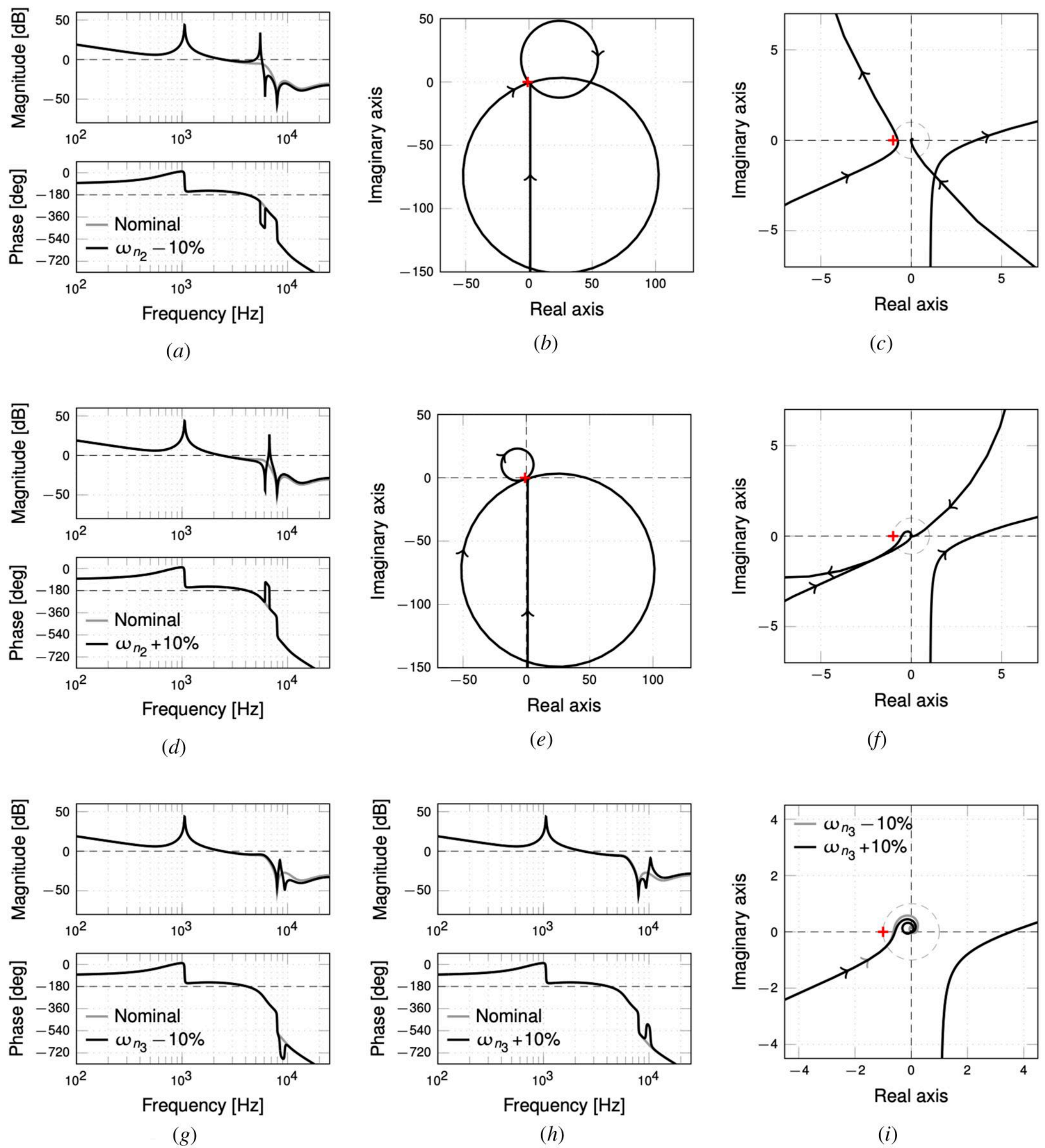

Figure 9. Robustness tests (Mirror 1): loop transfer function (Bode and Nyquist plots) for (a–f) a ±10% variation of the second resonance frequency, and (g–i) a ±10% variation of the third resonance frequency.

of Figures 9(a) and 9(d). However, only the +10% variation causes an instability, as evidenced by the encirclement of the critical point that appears in the Nyquist plot of Figures 9(*e*)–9(*f*). In contrast, with a −10% variation, the lobe on the Nyquist plot is completely rotated to the right, and no encirclement occurs around the critical point (see Figures 9(*e*)–9(*f*)). Given that the resonance frequencies increase with the actuation amplitude,[40] this potential instability poses a limitation to the proposed design. Nevertheless, robustness can be easily recovered by centering the notch filter on a frequency slightly larger than that of the targeted resonance, to better tolerate possible positive variations that might otherwise destabilize the loop. Variations in the other resonance frequencies do not pose significant stability issues: the first resonance, being within the control bandwidth, is phase stabilized even when perturbed, as long as an adequate phase margin is

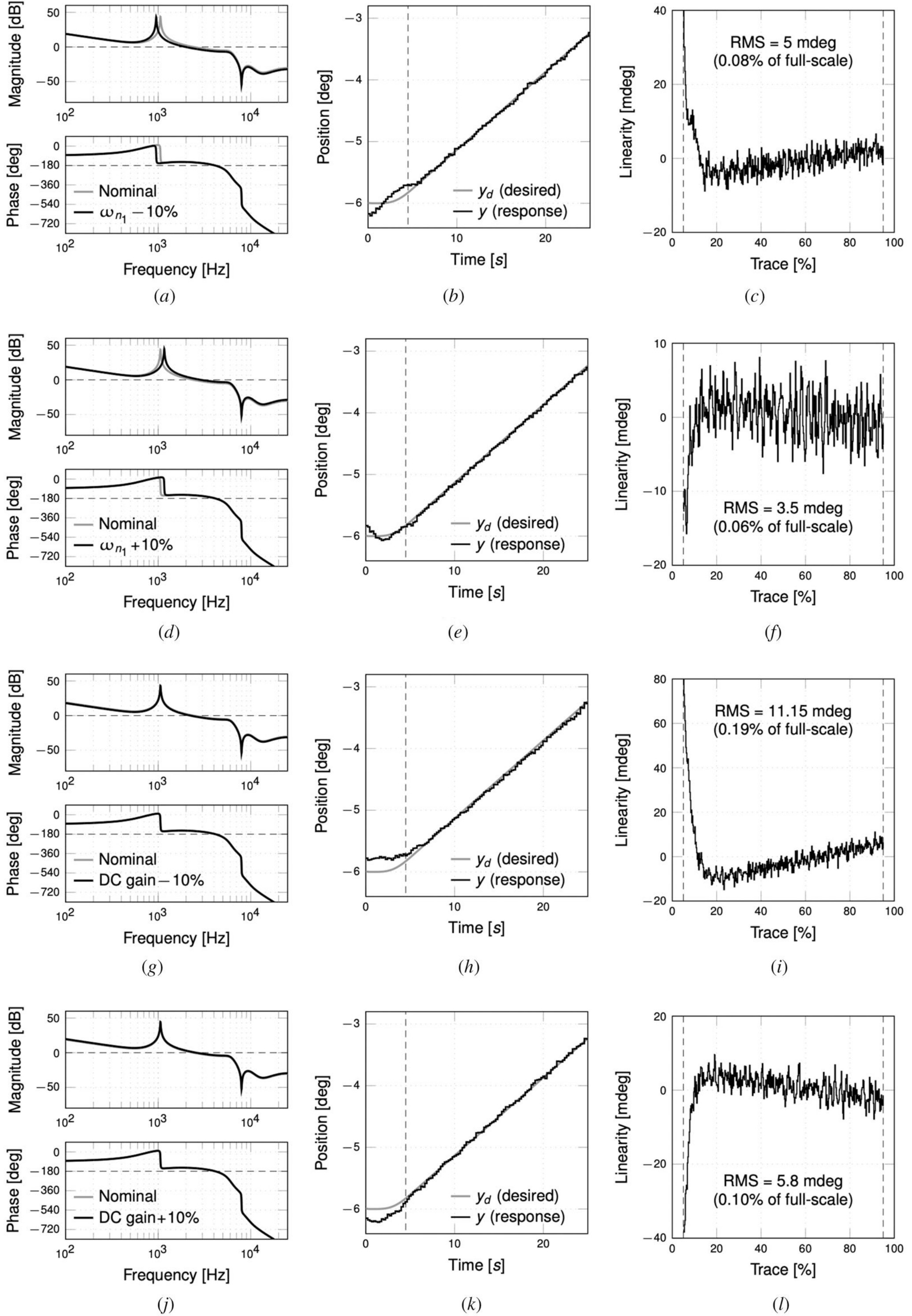

Figure 10. Robustness tests (Mirror 1): loop transfer function (Bode plots), control response detail and performance metrics (linearity error) for (a–c) a -10% variation of the first resonance frequency, (d–f) a $+10\%$ variation of the first resonance frequency, (g–i) a -10% variation of the DC gain, (j–k) a $+10\%$ variation of the DC gain.

maintained. The third instead remains well below the 0-dB line even in presence of variations, and is therefore gain stabilized by the feedback loop (see Figures 9(g)–9(i)).

Regarding the feedforward action, this is more sensitive to variations in the static gain and the first resonant frequency, as these parameters are used to design the command feedforward compensator $F_u(z)$. In particular, a -10% variation of the static gain has the effect of producing an under–compensation, resulting in an initial undershoot in the system response at the beginning of each trace (see Figure 10(h)). Conversely, a $+10\%$ variation produces an initial overshoot, as evidenced in Figure 10(k). Similar effects on the initial response are observed for variations of the first mechanical resonance (see Figure 10(b) and 10(e)). However, for $\pm10\%$ variations of the aforementioned parameters, the linear portion of trace remains almost unaffected, and performances are within specifications (see Figures 10(c), 10(f), 10(i), 10(l)).

5. Conclusions

This paper has presented a simple, yet effective solution for the closed-loop control of the angular deflection of linear micromirrors used in MEMS raster scanners for projection applications. The proposed design is particularly suited for the integration on custom hardware such as FPGA or ASIC, relying on a two degrees of freedom architecture with compensators that can be implemented with standard FIR or bi-quadratic IIR filter cells. The rather simple controller structure also reflects in a simplified tuning procedure. To facilitate this process, a rapid method for identifying the main system resonances has also been proposed. This information is required for the design of both the feedforward compensation, which aims to achieve the desired tracking performance while suppressing undesired ringing arising from the excitation of high-frequency resonances, and the feedback controller, which has to prevent potential mode spillover instabilities. The experimental results obtained on a rapid control prototyping testbed have shown that with a proper initial calibration, the proposed architecture is sufficient to attain the required performance specifications (evaluated in terms of linearity and reproducibility errors). In particular, there is no need for any extra compensation technique to cope with issues such as resonance ringing or actuator nonlinearity. However, in scenarios where the actuation or sensing systems exhibit a more severe nonlinear characteristic, it is expected that an auxiliary compensation strategy that relieves the workload of the feedback controller would produce better results. Among the available options, the Repetitive Control[43] and the Iterative Learning Control (ILC)[50] methodologies seem the most promising, considering also the repetitiveness of the control task, and certainly deserve to be analyzed in more depth in future works.

Disclosure statement

No potential conflict of interest was reported by the author(s).

ORCID

Riccardo Antonello http://orcid.org/0000-0003-4221-2004
Roberto Oboe http://orcid.org/0000-0003-3078-2915
Daniele D'Elia http://orcid.org/0009-0002-5454-7629
Luca Molinari http://orcid.org/0009-0009-8798-6311

References

[1] Solgaard, O.; Godil, A. A.; Howe, R. T.; Lee, L. P.; Peter, Y.-A.; Zappe, H. Optical MEMS: From micromirrors to complex systems. *J. Microelectromech. Syst.* **2014**, *23*, 517–538. DOI: 10.1109/JMEMS.2014.2319266.

[2] Tsai, C.-H.; Tsai, J.-C. MEMS optical switches and interconnects. *Displays* **2015**, *37*, 33–40. DOI: 10.1016/j.displa.2014.11.007.

[3] Stepanovsky, M. A comparative review of MEMS-based optical cross-connects for all-optical networks from the past to the present day. *IEEE Commun. Surv. Tutorials* **2019**, *21*, 2928–2946. DOI: 10.1109/COMST.2019.2895817.

[4] Liao, C-d.; Tsai, J-c The evolution of MEMS displays. *IEEE Trans. Ind. Electron.* **2009**, *56*, 1057–1065. DOI: 10.1109/TIE.2008.2005684

[5] Caprioli, M.; Roppolo, I.; Chiappone, A.; Larush, L.; Pirri, C. F.; Magdassi, S. 3D-printed self-healing hydrogels via digital light processing. *Nat. Commun.* **2021**, *12*, 2462. DOI: 10.1038/s41467-021-22802-z.

[6] Ma, J. Advanced MEMS-based technologies and displays. *Displays* **2015**, *37*, 2–10. DOI: 10.1016/j.displa.2014.10.003.

[7] Jung, I. W.; Lopez, D.; Qiu, Z.; Piyawattanametha, W. 2-d Mems scanner for handheld multispectral dual-axis confocal microscopes. *J. Microelectromech. Syst.* **2018**, *27*, 605–612. DOI: 10.1109/JMEMS.2018.2834549.

[8] Hwang, K.; Seo, Y.-H.; Jeong, K.-H. Microscanners for optical endomicroscopic applications. *Micro and Nano Syst. Lett.* **2017**, *5*, 1. DOI: 10.1186/s40486-016-0036-4.

[9] Pan, T.; Gao, X.; Yang, H.; Cao, Y.; Zhao, H.; Chen, Q.; Xie, H. A MEMS mirror-based confocal laser endomicroscope with image distortion correction. *IEEE Photonics J.* **2023**, *15*, 1–8. DOI: 10.1109/JPHOT.2023.3264597.

[10] Yoo, H. W.; Druml, N.; Brunner, D.; Schwarzl, C.; Thurner, T.; Hennecke, M.; Schitter, G. MEMS-based lidar for autonomous driving. *Elektrotech. Inftech.* **2018**, *135*, 408–415. DOI: 10.1007/s00502-018-0635-2.

[11] Wang, D.; Koppal, S. J.; Xie, H. A monolithic forward-view MEMS laser scanner with decoupled raster scanning and enlarged scanning angle for Micro LiDAR applications. *J. Microelectromech. Syst.* **2020**, *29*, 996–1001. DOI: 10.1109/JMEMS.2020.3001921.

[12] Wang, D.; Watkins, C.; Xie, H. MEMS mirrors for LiDAR: A review. *Micromachines.* **2020**, *11*, 456. DOI: 10.3390/mi11050456.

[13] Holzhüter, H.; Bödewadt, J.; Bayesteh, S.; Aschinger, A.; Blume, H. Technical concepts of automotive LiDAR sensors: A review. *OE.* **2023**, *62*, 031213. DOI: 10.1117/1.OE.62.3.031213.

[14] Kress, B. C. *Optical Architectures for Augmented-, Virtual-, and Mixed-Reality Headsets*, no. 316. Bellingham, Washington, USA. SPIE Press, 2020. DOI: 10.1117/3.2559304.

[15] Reitterer, J.; Chen, Z.; Balbekova, A.; Schmid, G.; Schestak, G.; Nassar, F.; Dorfmeister, M.; Ley, M. Ultra-compact micro-electro-mechanical laser beam scanner for augmented reality applications. In *Optical Architectures for Displays and Sensing in Augmented, Virtual, and Mixed Reality (AR, VR, MR) II*, vol. 11765, pp. 33–43. SPIE, 2021. DOI: 10.1117/12.2576704.

[16] Boni, N.; Carminati, R.; Mendicino, G.; Merli, M.; Terzi, D.; Lazarova, B.; Fusi, M. Piezoelectric MEMS mirrors for the next generation of small form factor AR glasses. In MOEMS and Miniaturized Systems XXI, vol. 12013. SPIE, 2022; pp. 30–46. DOI: 10.1117/12.2609863.

[17] Tauscher, J.; Davis, W. O.; Brown, D.; Ellis, M.; Ma, Y.; Sherwood, M. E.; Bowman, D.; Helsel, M. P.; Lee, S.; Coy, J. W. Evolution of MEMS scanning mirrors for laser projection in compact consumer electronics. In MOEMS and Miniaturized Systems IX, vol. 7594,. SPIE. 2010; pp. 84–95. DOI: 10.1117/12.843095.

[18] Bai, Y.; Yeow, J. T. W.; Constantinou, P.; Damaskinos, S.; Wilson, B. C. **2010**. A 2-d Micromachined Soi mems mirror with sidewall electrodes for biomedical imaging," *IEEE/ASME Trans. Mechatron.*, *15*, 501–510, DOI: 10.1109/TMECH.2010.2051451.

[19] Yalcinkaya, A.; Urey, H.; Brown, D.; Montague, T.; Sprague, R. Two-axis electromagnetic microscanner for high resolution displays. *J. Microelectromech. Syst.* **2006**, *15*, 786–794. DOI: 10.1109/JMEMS.2006.879380.

[20] Frigerio, P.; Diodoro, B. D.; Rho, V.; Carminati, R.; Boni, N.; Langfelder, G. Long-term characterization of a new wide-angle micromirror with PZT actuation and PZR sensing. *J. Microelectromech. Syst.* **2021**, *30*, 281–289. DOI: 10.1109/JMEMS.2021.3052448.

[21] Devasia, S.; Eleftheriou, E.; Moheimani, S. O. R. A survey of control issues in nanopositioning. *IEEE Trans. Contr. Syst. Technol.* **2007**, *15*, 802–823. DOI: 10.1109/TCST.2007.903345.

[22] Cao, Y.; Chen, X. B. A survey of modeling and control issues for piezo-electric actuators. *J. Dynam Syst. Measure. Control* **2015**, *137*, 014001. DOI: 10.1115/1.4028055.

[23] Schroedter, R.; Yoo, H. W.; Brunner, D.; Schitter, G. Charge-based capacitive self-sensing with continuous state observation for resonant electrostatic MEMS mirrors. *J. Microelectromech. Syst.* **2021**, *30*, 897–906. DOI: 10.1109/JMEMS.2021.3107797.

[24] Lei, H.; Wen, Q.; Yu, F.; Li, D.; Shang, Z.; Huang, J.; Wen, Z. AlN film based piezoelectric large-aperture MEMS scanning micromirror integrated with angle sensors. *J. Micromech. Microeng.* **2018**, *28*, 115012. DOI: 10.1088/1361-6439/aae051.

[25] Frigerio, P.; Carminati, R.; Molinari, L.; Langfelder, G. Piezoresistive versus piezoelectric position sensing in MEMS micromirrors: A noise and temperature drift comparison. *IEEE Sens. Lett.* **2022**, *6*, 1–4. DOI: 10.1109/LSENS.2022.3158385.

[26] Cheng, X.; Sun, X.; Liu, Y.; Zhu, L.; Zhang, X.; Zhou, L.; Xie, H. Integrated optoelectronic position sensor for scanning micromirrors. *Sensors* **2018**, *18*, 982. DOI: 10.3390/s18040982.

[27] Xia, C.; Qiao, D.; Zhang, Y.; Su, X.; Guo, Z. A position feedback solution based on the acoustic signal produced by electrostatically driven MEMS scanning mirror. In 2017 IEEE 12th International Conference on Nano/Micro Engineered and Molecular Systems (NEMS), 2017; pp. 558–561. DOI: 10.1109/NEMS.2017.8017084.

[28] Holmstrom, S. T. S.; Baran, U.; Urey, H. MEMS laser scanners: A review. *J. Microelectromech. Syst.* **2014**, *23*, 259–275. DOI: 10.1109/JMEMS.2013.2295470.

[29] Schroedter, R.; Roth, M.; Janschek, K.; Sandner, T. Flatness-Based Open-Loop and Closed-Loop Control for Electrostatic Quasi-Static Microscanners Using Jerk-Limited Trajectory Design. *Mechatronics* **2018**, *56*, 318–331. DOI: 10.1016/j.mechatronics.2017.03.005.

[30] Schroedter, R.; Janschek, K.; Sandner, T. Jerk and current limited flatness-based open loop control of Foveation scanning electrostatic micromirrors. *IFAC Proceedings Volumes* **2014**, *47*, 2685–2690. DOI: 10.3182/20140824-6-ZA-1003.02566.

[31] Sandner, T.; Grasshoff, T.; Schwarzenberg, M.; Schroedter, R.; Schenk, H. Quasistatic microscanner with linearized scanning for an adaptive three-dimensional laser camera. *J. Micro/Nanolith. MEMS. MOEMS.* **2014**, *13*, 011114. DOI: 10.1117/1.JMM.13.1.011114.

[32] Kyriakopoulos, K.; Saridis, G. Minimum Jerk Path generation. Proceedings. 1988 IEEE International Conference on Robotics and Automation. Philadelphia, PA: IEEE Computer Society Press, 1988. pp. 364–369. DOI: 10.1109/ROBOT.1988.12075.

[33] Sencer, B.; Tajima, S. Frequency optimal feed motion planning in computer numerical controlled machine tools for vibration avoidance. *J. Manufactur. Sci. Eng.* **2017**, *139*, 2017, 011006. DOI: 10.1115/1.4034140.

[34] Janschek, K.; Sandner, T.; Schroedter, R.; Roth, M. Adaptive prefilter design for control of quasistatic microscanners. *In IFAC Proceedings Volumes* **2013**, *46*, 197–206. DOI: 10.3182/20130410-3-CN-2034.00112.

[35] Barrett, L. K.; Imboden, M.; Javor, J.; Campbell, D. K.; Bishop, D. J. Feedforward control algorithms for MEMS Galvos and scanners. *J. Microelectromech. Syst.* **2021**, *30*, 612–621. Aug DOI: 10.1109/JMEMS.2021.3074301.

[36] Singer, N. C.; Seering, W. P. Preshaping command inputs to reduce system vibration. *J. Dynam. Syst. Measurement. Control* **1990**, *112*, 76–82. DOI: 10.1115/1.2894142.

[37] Schitter, G.; Thurner, P. J.; Hansma, P. K. Design and input-shaping control of a novel scanner for high-speed atomic force microscopy. *Mechatronics* **2008**, *18*, 282–288. DOI: 10.1016/j.mechatronics.2008.02.007.

[38] Milanović, V.; Kasturi, A.; Yang, J.; Hu, F. Closed-loop control of gimbal-less MEMS mirrors for increased bandwidth in LiDAR applications. In M. D. Turner and G. W. Kamerman, Eds., Anaheim, California, United States, May 2017; p. 101910N. DOI: 10.1117/12.2264069.

[39] Tsai, C.-C.; Li, Z.-H.; Lin, Y.-T.; Lu. M. S.-C. A closed-loop controlled CMOS MEMS biaxial scanning mirror for projection displays. *IEEE Sensors J.* **2020**, *20*, 242–249. DOI: 10.1109/JSEN.2019.2942331.

[40] Frigerio, P.; Molinari, L.; Barbieri, A.; Zamprogno, M.; Mendicino, G.; Boni, N.; Langfelder, G. "Nested Closed-Loop Control of Quasi-Static MEMS Scanners With Large Dynamic Range,". *IEEE Trans. Ind. Electron.* **2023**, *70*, 4217–4225. DOI: 10.1109/TIE.2022.3174235.

[41] Frigerio, P.; Cozzi, S.; Molinari, L.; Barbieri, A.; Carminati, R.; Merli, M.; Langfelder, G. On the use of Kalman filters for high-order mode rejection in PZT-based microscanners. *J. Micromech. Microeng.* **2023**, *33*, 044002. DOI: 10.1088/1361-6439/acbda8.

[42] Schroedter, R.; Schwarzenberg, M.; Dreyhaupt, A.; Barth, R.; Sandner, T.; Janschek, K. Microcontroller based closed-loop control of a 2D Quasi-Static/Resonant Microscanner with on-Chip Piezo-resistive sensor feedback. W. Piyawattanametha and Y.-H. Park, Eds., San Francisco, California, United States, Feb 2017; p. 1011605. DOI: 10.1117/12.2251802.

[43] Schroedter, R.; Schwarzenberg, M.; Grahmann, J.; Sandner, T.; Janschek, K. Repetitive nonlinear control for linear scanning micro mirrors. In MOEMS and Miniaturized Systems XVII, vol. 10545. SPIE, Feb 2018; pp. 234–241. DOI: 10.1117/12.2285558.

[44] Frigerio, P.; Tarsi, R.; Molinari, L.; Maiocchi, G.; Barbieri, A.; Langfelder, G. A Novel closed-loop architecture for accurate Micromirror Trajectory control in linear scanning MEMS-based projectors. In MOEMS and Miniaturized Systems XX. SPIE, Mar 2021; p. 4. DOI: 10.1117/12.2577186.

[45] Frigerio, P.; Molinari, L.; Barbieri, A.; Carminati, R.; Boni, N.; Langfelder, G. Closed-Loop Control of Quasi-Static Scanning PZT Micromirrors with Embedded Piezoresistive Sensing and Spurious Mode Rejection. In 2021 21st International Conference on Solid-State Sensors, Actuators and Microsystems (Transducers), Jun 2021; pp. 435–438. DOI: 10.1109/Transducers50396.2021.9495680.

[46] Söderström, T.; Stoica, P. *System identification*. Prentice-Hall, Inc., USA, 1988.

[47] Preumont, A. *Vibration control of active structures*, 3rd ed., vol. 179. Dordrecht: Springer Netherlands, 2011. DOI: 10.1007/978-94-007-2033-6.

[48] Åström, K. J.; Wittenmark, B. *Computer-Controlled Systems* (3rd Ed.). Prentice-Hall, Inc., USA, 1997.

[49] Vergara, A.; Tsukamoto, T.; Fang, W.; Tanaka, S. Feedback controlled Pzt Micromirror with integrated buried piezoresistors. in 2022 IEEE 35th International Conference on Micro Electro Mechanical Systems Conference (MEMS). Tokyo, Japan: IEEE, Jan 2022; pp. 243–246. DOI: 10.1109/MEMS51670.2022.9699754.

[50] Macho, M.; Yoo, H. W.; Schroedter, R.; Schitter, G. Iterative learning control for Quasi-Static MEMS Mirror with Switching Operation. in 2023 IEEE 36th International Conference on Micro Electro Mechanical Systems (MEMS), Jan 2023; pp. 538–541. DOI: 10.1109/MEMS49605.2023.10052637.